Optimal ultra-miniature polarimeters in silicon photonic integrated circuits

Zhongjin Lin, Leslie A. Rusch, Yuxuan Chen, and Wei Shi

Optimal ultra-miniature polarimeters in silicon photonic integrated circuits

Zhongjin Lin,[1] Leslie A. Rusch,[1] Yuxuan Chen,[1] and Wei Shi[1, a)]

Department of Electrical and Computer Engineering, Center of Optics, Photonics and Laser (COPL), Université Laval, Québec, QC, Canada G1V 0A6

(Dated: 25 September 2019)

Measurement of the state of polarization of light is essential in a vast number of applications, such as quantum and classical communications, remote sensing, astronomy, and biomedical diagnostics. Nanophotonic structures and integrated photonic circuits can, in many circumstances, replace conventional discrete optical components for miniature polarimeters and chip-scale polarimetry systems, and thus significantly improve robustness while minimizing footprint and cost. We propose and experimentally demonstrate two silicon photonic (SiP) four-photodetector (PD) division-of-amplitude polarimeters (4PD-DOAPs) using a CMOS-compatible photonic fabrication process. The first design targets minimizing the number of optical components. The second design makes use of a slightly more complex circuit design to achieve an optimal frame for measurements; this measurement frame minimizes and equalizes estimation variances in the presence of the additive white Gaussian noise and the signal dependent shot noise. Further theoretical examination reveals that within the optimal measurement frames for Stokes polarimeters, the DOAP with four PDs has the minimal equally-weighted variance compared to those with a greater number of PDs.

I. INTRODUCTION

State of polarization (SoP) is one of the essential properties of light. It conveys unique information on optical sources and on light-matter interactions[1–4]. Measurement of SoP thus finds crucial application in communications, quantum information, astronomy, and biomedical and chemical sensing[5]. Polarimeter performance has been improved over and again during its long development history[6]. While theory on optimization of polarimeter parameters is well established, the implementation of polarimeters in bulky, discrete optical components has hindered their broad application.

Recently, the rapid development of nanoscience and nanotechnology has led to a significant progress towards ultra-miniaturization of polarimeters. Some miniature polarimeters have been demonstrated, such as a metasurface polarimeter[7–9], a circular polarization imager using chiral structure[10], all-fiber polarimeter[11], and a sub-wavelength polarimeter exploiting the spin-orbit interaction of light[12]. The photonic integrated circuit (PIC) technology has immense advantages for realizing miniature, solid-state polarimeters as it is capable of integrating a vast number of optical components on a single chip[13–16].

A complete chip-scale polarimetry system can be achieved with all the components, including photo-detectors (PDs) and electric signal processing circuits, integrated on micro-chips, leading to substantially improved robustness with reduced cost and footprint. Various materials can be adopted in PICs, such as indium phosphide[17], silicon[13,18], silicon nitride[19], and germanium[20], covering from visible to long-wave-infrared regions, while sharing the same principles and waveguide architectures. We recently demonstrated a chip-scale full-Stokes polarimeter in a silicon PIC, consisting of a surface polarization splitter (SPS) and an on-chip optical interferometer circuit, producing the complete analysis matrix of an optimally conditioned polarimeter[21]. Silicon photonic Stokes

receivers[22,23] were also demonstrated using integrated waveguide components such as an edge coupler, a polarization splitter, an optical hybrid, and Ge PDs .

However, compared to conventional solutions, optimization of the PIC-based polarimeter parameters has not been extensively explored, which will be addressed in this paper. We use integrated optical components to realize an optimal PIC-based polarimeter with the CMOS-compatible silicon photonics technology. Our design achieves classical optimal measurement frames for SoP reconstruction.

Here we focus on division-of-amplitude polarimeters (DOAPs) that split the light beam into several paths for fast, simultaneous measurement[24]. In our previous work, we proposed and demonstrated an optimally conditioned silicon photonic DOAP[21] requiring six PDs. Nevertheless, the full reconstruction of the Stokes vector in principle requires only four measurements of optical intensity. Therefore, the signal processing cost was increased as we generated more measurements than the minimal four for a DOAP. In this paper, we propose two chip-scale silicon photonic four-photodetector DOAPs (SiP-4PD-DOAPs). The first design minimizes the number of optical components for an ultra-compact design. The second exploits an asymmetrical power splitter (APS)[25] to produce an optimal reference frame with minimized and equalized estimation variances. Both devices are designed for a standard 220-nm-thick silicon-on-insulator (SOI) wafer and are optimal in the presence of both additive Gaussian noise and signal-dependent (Poisson) shot noise.

The rest of this paper is organized as follows. In Section II, we review the fundamentals of Stokes polarimeters and define conventions that will be used in the following sections. In Section III and IV, we present the design and experimental results of the two proposed SiP-4PD-DOAPs. While photodiodes were not integrated in the device under test, our results clearly establish the viability of an ultra-compact solution. In Section V, we discuss various structures for noise minimization in the scope of optimal measurement frames of Stokes polarimeters. Section VI is the conclusion.

———————
a)Electronic mail: wei.shi@gel.ulaval.ca

II. STOKES POLARIMETER PRINCIPLES

The SoP is typically characterized by a 4×1 Stokes vector. Therefore, complete reconstruction of the SoP requires a minimum of four distinct measurements, which can be realized by projecting the Stokes vector onto four or more analysis states determined by the Mueller matrix (analysis matrix) of the polarimeter. In classical free-space optical systems, this operation can be achieved via rotating polarizers or via retarders in combination of a fixed polarizer. In a PIC, this can be realized through waveguide interferometers without mechanical moving parts.

Figure 1 shows PIC counterparts of some free-space optical components commonly used in Stokes polarimeters. A SPS[21] can decompose the two orthogonal E-field components ($\mathbf{E}_x$ and $\mathbf{E}_y$), each coupling (ideally with equal power) into two single-mode waveguides that guide in opposite directions. As shown in Fig. 1a, the SPS functions as combined polarization beam splitter (PBS) and half-wave plate (HWP) in a conventional free-space optical system. An on-chip beam combiner (i.e., 3-dB Y-branch[26]) coherently combines $\mathbf{E}_x$ and $\mathbf{E}_y$ (orthogonal in free space, but coupled to the same mode in two waveguides), as shown in Fig. 1b, outputting $\frac{\sqrt{2}}{2}(\mathbf{E_x} + \mathbf{E_y})$, which is equivalent to a $45°$ linear polarizer. A retarder can be simply replaced by two optical waveguides with various lengths that introduce an phase difference between $\mathbf{E}_x$ and $\mathbf{E}_y$ (as shown in Fig. 1c).

A polarimeter transforms the Stokes vector into a series of intensities that can be detected by PDs. The analysis matrix $\mathbf{W}$ defines the transformation

$$\mathbf{I} = \mathbf{W} \cdot \mathbf{S} + \mathbf{n}, \tag{1}$$

where $\mathbf{S} = (S_0, \ S_1, \ S_2, \ S_3)^T$ is the input Stokes vector. $\mathbf{I} = (I_1, \ I_2, ..., \ I_N)^T$ is an N-dimensional vector representing the measured intensities, not to be confused with the identity matrix. The noise contribution of the PDs is $\mathbf{n}$. The estimated Stokes vector $\hat{\mathbf{S}}$ is given by

$$\hat{\mathbf{S}} = \mathbf{W}^\dagger \cdot \mathbf{W} \cdot \mathbf{S} + \mathbf{W}^\dagger \cdot \mathbf{n}, \tag{2}$$
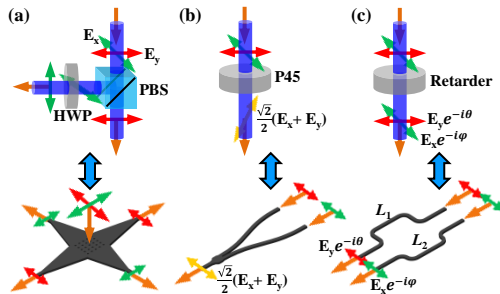

FIG. 1. Traditional element (top) and PIC counterpart (bottom) of a) a SPS, b) a 3 dB Y-branch, and c) phase-retarded waveguides. Top: PBS, polarizing beam splitter; P45, polarizer at $45°$ with respect to the x-axis. Bottom: electric field along the x-axis (y-axis) in green (red) double-headed arrows; orange single-headed arrows point in the propagation direction.

where $\mathbf{W}^\dagger$ denotes the generalized inverse of $\mathbf{W}$, also known as the synthesis matrix. Here, we only consider the case of $N = 4$, so that $\mathbf{W}^\dagger = \mathbf{W}^{-1}$. The error of the estimated Stokes vector can be obtained by

$$\Delta\mathbf{S} = \hat{\mathbf{S}} - \mathbf{S} = \mathbf{W}^{-1} \cdot \mathbf{n}. \tag{3}$$

Equation (3) shows estimation error is influenced by noise level and the synthesis matrix. For noise $\mathbf{n}$ with covariance matrix Γ, taking expectations, we have

$$\mathrm{Cov}\left(\hat{\mathbf{S}}\right) = E\{\Delta\mathbf{S}(\Delta\mathbf{S})^T\} = \mathbf{W}^{-1}\Gamma\left(\mathbf{W}^{-1}\right)^T. \tag{4}$$

In the presence of additive white Gaussian noise (AWGN), and when the noise at each PD is zero-mean and identically distributed with variance σ_n^2, we have

$$\mathrm{Cov}\left(\hat{\mathbf{S}}\right) = \sigma_n^2\mathbf{W}^{-1}\left(\mathbf{W}^{-1}\right)^T. \tag{5}$$

The condition number[27,28] $\kappa = \|\mathbf{W}\| \cdot \|\mathbf{W}^{-1}\|$ is a figure of merit often used to evaluate polarimeter performance, where $\|*\|$ is the matrix norm (taken as the L_2 norm throughout this work). The detection signal-to-noise ratio (SNR) is maximized when the condition number is minimized.

In the presence of shot noise (*i.e.*, Poisson noise), assuming independent noise in each PD, the noise covariance matrix is diagonal with i^{th} entry proportional to the ith detected signal power. For $\mathbf{A}_{ij}$ denoting the i, j element of matrix $\mathbf{A}$, this means

$$\Gamma_{i,i} \propto (\mathbf{WS})_i. \tag{6}$$

Therefore, the variance of the Stokes estimate is SoP dependent for Poisson noise. As the signal power varies across PDs, the Poison noise is not identically distributed (unlike the AWGN). For best performance, the polarimeter would equalize the noise variances.

Following[29], we define matrix Q by

$$Q_{ij} = \sum_{n=1}^{4} \left[\mathbf{W}_{(i+1)n}^{-1}\right]^2 \mathbf{W}_{n(j+1)}, \tag{7}$$

$\mathbf{u}^i = (Q_{i1}, \ Q_{i2}, \ Q_{i3})^T$, and P as the degree of polarization. As the Poison variance depends on $\mathbf{S}$, each component of $\hat{\mathbf{S}}$ will have some maximum variance, γ_i^{max}, and minimum variance, γ_i^{min}, associated with that component. The mean excursion between these extrema, $\Delta\gamma$, is given by

$$\Delta\gamma = \frac{1}{3} \cdot \sum_{n=1}^{3} \left(\gamma_i^{max} - \gamma_i^{min}\right) = \frac{2}{3}S_0 P \sum_{n=1}^{3} \|\mathbf{u}^i\|, \tag{8}$$

Ideally the polarimeter would equalize the noise for zero excursion, *i.e.*, where maximum noise variance γ_i^{max} equal to minimum noise variance γ_i^{min} on each Stokes vector component. We therefore seek an optimal structure[29] minimizing the condition number κ and the variance difference $\Delta\gamma$.
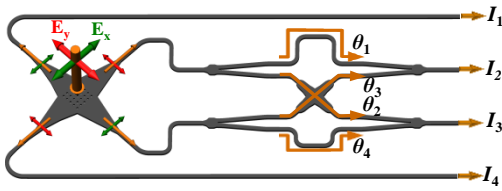
FIG. 2. The schematic of the proposed SiP-4PD-DOAP: θ_1, θ_2, θ_3, and θ_4 are the phased variations at each paths; I_1, I_2, I_3, and I_4 are the intensities of output.

III. ULTRA-COMPACT DOAP

A. Design

The schematic of the proposed SiP-4PD-DOAP is shown in Fig. 2. Firstly, the incoming light is split into four waveguides by SPS. The optical waves propagating in the four paths (i.e., $\frac{\sqrt{2}}{2}\mathbf{E_x}$, $\frac{\sqrt{2}}{2}\mathbf{E_y}$, $\frac{\sqrt{2}}{2}\mathbf{E_x}$, and $\frac{\sqrt{2}}{2}\mathbf{E_y}$) carry the full information of SoP of the incoming light. Two of the optical paths are split into four paths by two 50:50 Y-branches, and then they separately pass through unique θ_i-phase-retard waveguides.

The optical waves which pass through θ_1-phase-retard and θ_3-phase-retard waveguides are by construction coherent with each other and they combine to yield intensity I_2. The optical waves passing through θ_2-phase-retard and θ_4-phase-retard waveguides are also coherent, yielding I_3. This section of the polarimeter is called a crossing coherent analyzer.

The remaining paths do not pass through any components. A 3-dB optical attenuator is added before the PDs to distribute unpolarized light equally among the four outputs, intensities I_1 through I_4.

The analysis matrix $\mathbf{W}_1$ of the proposed SiP-4PD-DOAP is therefore

$$\mathbf{W}_1 \propto \frac{1}{8}\begin{pmatrix} 1 & 1 & 0 & 0 \\ 1 & 0 & \cos(\theta_1-\theta_3) & -\sin(\theta_1-\theta_3) \\ 1 & 0 & \cos(\theta_4-\theta_2) & \sin(\theta_4-\theta_2) \\ 1 & -1 & 0 & 0 \end{pmatrix}. \quad (9)$$

We plot the condition number for this polarimeter as a function with $(\theta_1-\theta_3)$ and $(\theta_4-\theta_2)$ in Fig. 3. The minimum condition number can be obtained when

$$(\theta_1-\theta_3+\theta_4-\theta_2) = (2m\pm0.365)\pi, \quad (10)$$

where m is any integer.

We next improve the device by minimizing $\Delta\gamma$, or equivalently, minimizing $\Delta\widetilde{\gamma} = \sum_{n=1}^{3}\|\mathbf{u}^i\|$. The variation of $\Delta\widetilde{\gamma}$ with θ_{up} for Eq. (10) is depicted in Fig. 4. For the $m=0$ case, we observe minimum $\Delta\widetilde{\gamma}$ at $(\theta_1-\theta_3) = 0.1825\pi$ or 0.3175π. For our design, we selected $(\theta_1-\theta_3) = 0.1825\pi$; see arrow in Fig. 4. The experimental characterization of this SiP-DOAP is discussed in section 3. The analysis matrix $\mathbf{W}_a$ is

$$\mathbf{W}_a \propto \frac{1}{8}\begin{pmatrix} 1 & 1 & 0 & 0 \\ 1 & 0 & 0.84 & -0.542 \\ 1 & 0 & 0.84 & 0.542 \\ 1 & -1 & 0 & 0 \end{pmatrix}. \quad (11)$$
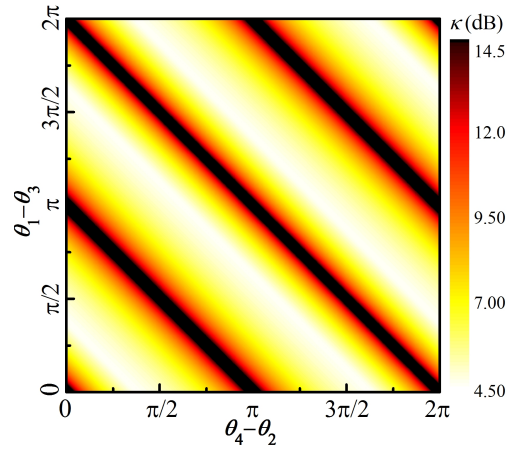

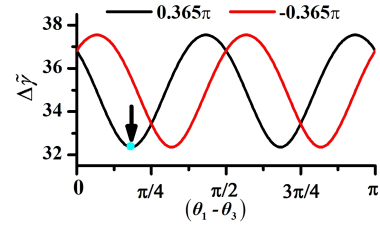FIG. 3. Condition number in dB vs. $(\theta_1-\theta_3)$ and $(\theta_4-\theta_2)$.

FIG. 4. Noise variance excursion $\Delta\widetilde{\gamma}$ vs. $(\theta_1-\theta_3)$ with $(\theta_4-\theta_2)$ determined by Eq. (10) for $m=0$ (plus value in black, minus value in red). Arrow indicates choice for fabricated device.

B. Experiment and results

The device was fabricated using a commercial CMOS-compatible SOI process with electron-beam lithography at Applied Nanotools Inc. The thicknesses of the silicon and oxide layers are 220 nm and 2 μm, respectively. The scanning electron microscope (SEM) image of the fabricated devices is presented in Fig. 5a. The size of the strip waveguides are 500 nm $\times$ 220 nm. The SPS is formed using a 30×30 array of cylindrical holes fully etched through silicon with a period Λ of 695 nm and a hole diameter D of 440 nm (as shown in the inset of Fig. 5a). The geometry of this 2-D array is based on the Huygens–Fresnel principle. When the period of the cylindrical holes matches the Bragg condition for a certain wavelength, the light with normal incidence can be coupled into the waveguide[30].

We define the numerical efficiency by

$$(P_{x1}+P_{x2}+P_{y1}+P_{y2})/P_0 \quad (12)$$

where P_0 is the incident optical power, and P_{x1}, P_{x2}, P_{y1}, P_{y2} are the optical power coupled into the four paths, respectively. The SPS numerical efficiency is given in Fig. 5b. Its 3-dB bandwidth is 35 nm, and the center wavelength is 1550 nm. More details about the design of SPS are shown in our previous paper[21].

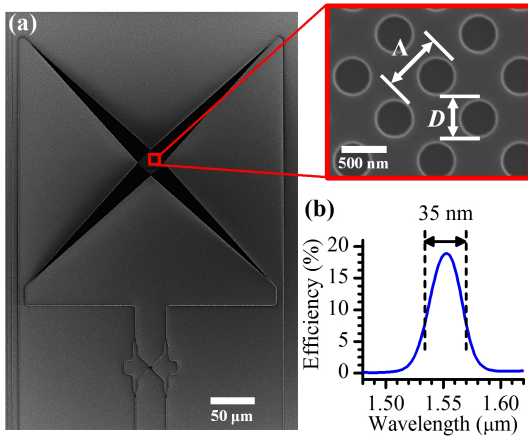The experiment setup is shown in Fig. 6. A linearly polarized light beam is generated using a tunable laser. The

FIG. 5. (a) The scanning electron microscope (SEM) image of the fabricated device.The insets show the enlarged images of the SPS and the cross section. (b) The numerical efficiency of the SPS as a function with wavelength.
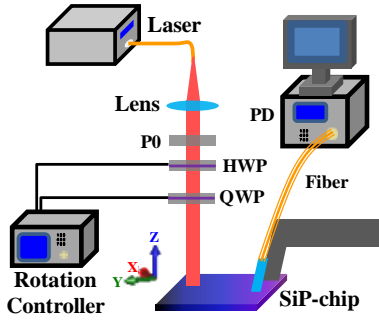

FIG. 6. The schematic of the experimental setup. P0, polarizer with orientation at $0°$ with respect to the x-axis. HWP, half-wave plate. QWP, quarter-wave plate. PD, photo-detector.

SoP is controlled by a polarizer (650-2000 nm, Thorlabs), an HWP (1550 nm, Thorlabs), and a quarter-wave plate (QWP, 1550 nm, Thorlabs). The orientation of polarizer is fixed at $0°$ with respect to the x-axis. Rotating the HWP and QWP we can generate any SoPs. Two stepper motor rotations (K10CR1/M, Thorlabs) are separately used to control the angles of the HWP and QWP. The four output ports of the on-chip polarimeter are readout using off-chip photodetectors through the fibers.

Through randomly rotating the HWP and QWP, we can generate a series of SoPs that spread widely over the surface of Poincaré sphere, as shown in Fig. 7a and b. The fabricated device was used to measure these SoPs. The measured results and the corresponding input SoPs are depicted in Fig. 7c. An excellent agreement is observed between the measured and input SoPs. Because our device is unpackaged, the experimental set-up vibrations would cause near 0.8-dB of intensity measurement relative errors, which would bring near 0.114 of root-mean-square (RMS) error of the SoP measurements[21]. Therefore, the RMS error of the Stokes vector reconstruction is very high and achieves 0.147 in this demonstration. The RMS error can be significantly reduced after packaging or us-

ing integrated PDs[31,32] on the chip.

To study the property of our device responds to other wavelengths, we fix the orientations of HWP and QWP at $20°$ and $60°$ with respect to the x-axis, respectively, and tune the wavelength from 1540 nm to 1565 nm. The input SoPs as a function with wavelength are shown in the dashed line of Fig. 8. The dots with error bar in the Fig. 8 are the measured results of our device. We can observe that the measured results also agree well with the corresponding input SoPs at other wavelengths.

IV. DOAP WITH MINIMIZED INFLUENCE OF NOISE

A. Design

The condition number of the above device (shown in Fig.5) is $1.65\sqrt{3}$, which is higher than the theoretical minimum value for a full-Stokes polarimeter[27]. The noise variances of each Stokes element estimate are sensitive to the incoming SoP in the presence of signal-dependent Poisson shot noise[29]. To obtain a minimal and equalized noise variance on each Stokes channel, another structure is proposed and presented in Fig. 9. It includes two crossing coherent analyzers and two APS. The APS are located between the SPS and crossing coherent analyzer. The schematic of APS is presented in Fig. 10a. For APS, we denote the values of the weaker and the relatively stronger output power ratio by PR and $(1-PR)$, respectively. The length (L) and width ($2w$) of the splitting region of APS are equal to 2.32 μm and 1.4 μm, respectively. Controlling the asymmetry of APS[25], we can control the output power ratio PR. Besides, a 2-ports SPS is designed to replace the 4-ports SPS. To increase the efficiency of the 2-ports SPS, two distributed Bragg reflection (DBR) gratings[33] are added at two idle ports of SPS. DBR gratings can reflect the lights back to the desired waveguides.

As shown in Fig. 9, we set the variations of the phase in crossing coherent analyzer as θ_1', θ_2', θ_3', and θ_4', respectively. And the intensities of the output ports are defined as I_1', I_2', I_3', and I_4', respectively.The analysis matrix $\mathbf{W}_2$ of this device can be obtained by

$$\mathbf{W}_2 \propto \frac{1}{4}\begin{pmatrix} 1 & -a_1 & a_2\cos(\theta_4'-\theta_2') & -a_2\sin(\theta_4'-\theta_2') \\ 1 & -a_1 & a_2\cos(\theta_1'-\theta_3') & a_2\sin(\theta_1'-\theta_3') \\ 1 & a_1 & a_2\cos(\theta_1'-\theta_3') & -a_2\sin(\theta_1'-\theta_3') \\ 1 & a_1 & a_2\cos(\theta_4'-\theta_2') & a_2\sin(\theta_4'-\theta_2') \end{pmatrix},$$

(13)

where $a_1 = (1-\tau)/(1+\tau)$, $a_2 = 2\sqrt{\tau}/(1+\tau)$, and $\tau = PR/(1-PR)$. According to work by Goudail[29], we know there are only two analysis matrices (within arbitrary row permutations) which have the properties of $\kappa = \sqrt{3}$ and $\Delta\gamma = 0$. The two analysis matrices $\mathbf{W}_b$ and $\mathbf{W}_{b'}$ have the formula that

$$\mathbf{W}_b \propto A\begin{pmatrix} 1 & -\frac{1}{\sqrt{3}} & -\frac{1}{\sqrt{3}} & -\frac{1}{\sqrt{3}} \\ 1 & -\frac{1}{\sqrt{3}} & \frac{1}{\sqrt{3}} & \frac{1}{\sqrt{3}} \\ 1 & \frac{1}{\sqrt{3}} & \frac{1}{\sqrt{3}} & -\frac{1}{\sqrt{3}} \\ 1 & \frac{1}{\sqrt{3}} & -\frac{1}{\sqrt{3}} & \frac{1}{\sqrt{3}} \end{pmatrix},$$
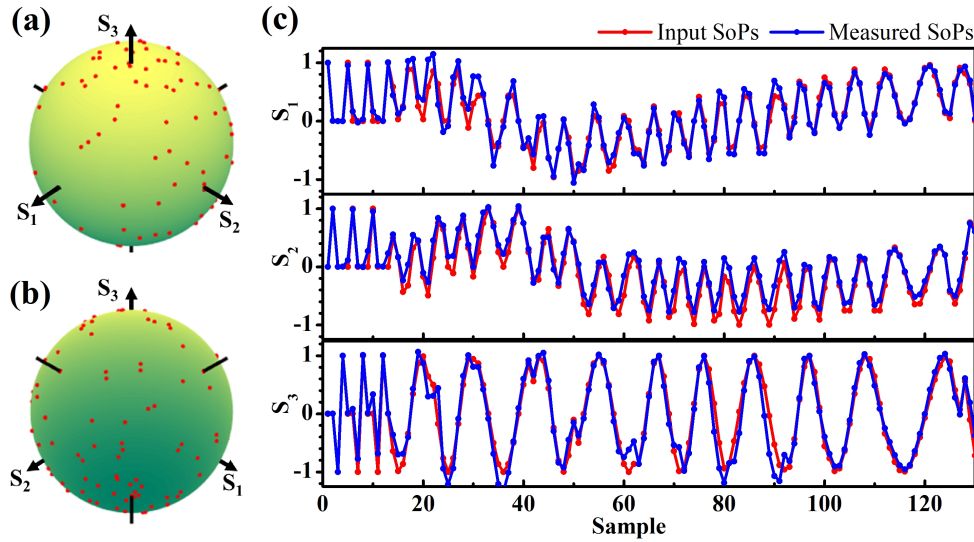
(14)

FIG. 7. (a) and (b) are front and back views of Poincaré sphere. Red dots represent the measured polarization state. (c) The measured results of our device and their corresponding input SoPs at the wavelength of 1550 nm.
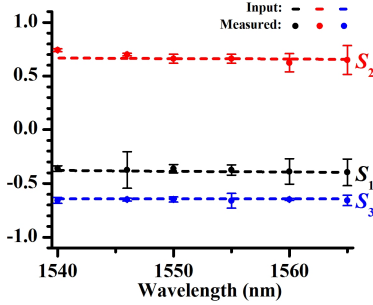

FIG. 8. The measured results of our device and their corresponding input SoPs under the different wavelengths, when the orientations of HWP and QWP are fixed at $20°$ and $60°$ with respect to the x-axis, respectively.

and

$$\mathbf{W}_{b'} \propto A \begin{pmatrix} 1 & -\frac{1}{\sqrt{3}} & \frac{1}{\sqrt{3}} & -\frac{1}{\sqrt{3}} \\ 1 & -\frac{1}{\sqrt{3}} & -\frac{1}{\sqrt{3}} & \frac{1}{\sqrt{3}} \\ 1 & \frac{1}{\sqrt{3}} & -\frac{1}{\sqrt{3}} & -\frac{1}{\sqrt{3}} \\ 1 & \frac{1}{\sqrt{3}} & \frac{1}{\sqrt{3}} & \frac{1}{\sqrt{3}} \end{pmatrix}, \quad (15)$$

where A is a positive value ($0 < A \leq 1/2$), and here, $A = 1/4$. Comparing Eqs. (13) with (14) and (15), we can obtain that when $\tau = 2 - \sqrt{3}$, the condition number of our device would have the potentiality that achieving a optimal performance. When $\tau = 2 - \sqrt{3}$, the condition number as a function with $(\theta'_1 - \theta'_3)$ and $(\theta'_4 - \theta'_2)$ is presented in Fig. 10. Figure 10 shows that when $(\theta'_1 - \theta'_3) = 2n\pi \pm \pi/4$ and $(\theta'_4 - \theta'_2) = 2n\pi \pm 3\pi/4$, or $(\theta'_1 - \theta'_3) = 2n\pi \pm 3\pi/4$ and $(\theta'_4 - \theta'_2) = 2n\pi \pm \pi/4$ (where n is an integer), the optimal condition number ($\sqrt{3}$) can be obtained. The analysis $\mathbf{W}_b$ can be achieved when $(\theta'_1 - \theta'_3) = \pi/4$ and $(\theta'_4 - \theta'_2) = 3\pi/4$. And The analysis $\mathbf{W}_{b'}$ can be achieved when $(\theta'_1 - \theta'_3) =$

$3\pi/4$ and $(\theta'_4 - \theta'_2) = \pi/4$. In the conventional free-space optical system, such polarimeters have been realized via using two variable retarders[34]. But in the PIC system, as far as we know, we are the first ones who propose such polarimeters. The device proposed by Martínez, et al.,[12] was only optimized in the presence of additive white Gaussian noise (i.e. $\kappa = \sqrt{3}$ but $\Delta\gamma > 0$). Besides, their device needs a polarization splitter/filter at each output, which will make condition number larger than $\sqrt{3}$.

B. Experiment and results

Here, we choose the structure of $(\theta'_1 - \theta'_3) = 3\pi/4$, $(\theta'_4 - \theta'_2) = \pi/4$, and $\tau = (2 - \sqrt{3})$ for experimental demonstration. Note that it is not the only structure which has the minimum influence of noise. As shown in Fig. 10(b), the coordination of $(\pi/4, 3\pi/4)$, $(3\pi/4, \pi/4)$, $(5\pi/4, 7\pi/4)$, and $(7\pi/4, 5\pi/4)$ in principle should all have the minimum condition number.

The SEM image of the improved device with a footprint of $350 \times 460~\mu m^2$ is presented in Fig. 11a. The enlarged SEM images of APS and SPS are shown in Fig. 11 b and c, respectively. In Fig. 11 c, we can observe that the DBR consists of 8 alternating layers of silicon and silicon oxide. The width of silicon layer, and the lattice period are 160 nm, and 360 nm, respectively. The improved device were used to measure a series of SoPs, and the corresponding results are depicted in Fig. 11 d. The measured results agree well with the input SoPs. Its RMS error is near 0.081 which is 44 % lower than that of the unimproved device under the same 0.8-dB of intensity measurement relative errors caused by the vibrations of the experimental set-up. Next, we will discuss the architecture of polarimeter with the measurement frame.
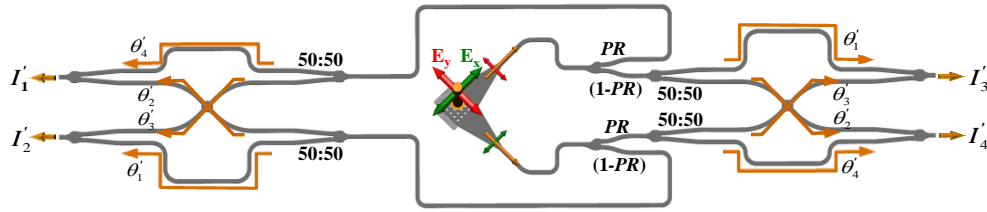
FIG. 9. The schematic of the improved SiP-4PD-DOAP. θ_1, θ_2', θ_3', and θ_4' are the phased variations at each path. I_1', I_2', I_3', and I_4' are the intensities of output. The power splitters with power ratio PR and $(1 - PR)$ are the asymmetrical power splitters (APSs). The power splitters located near the text of $50:50$ are the symmetrical power splitters.
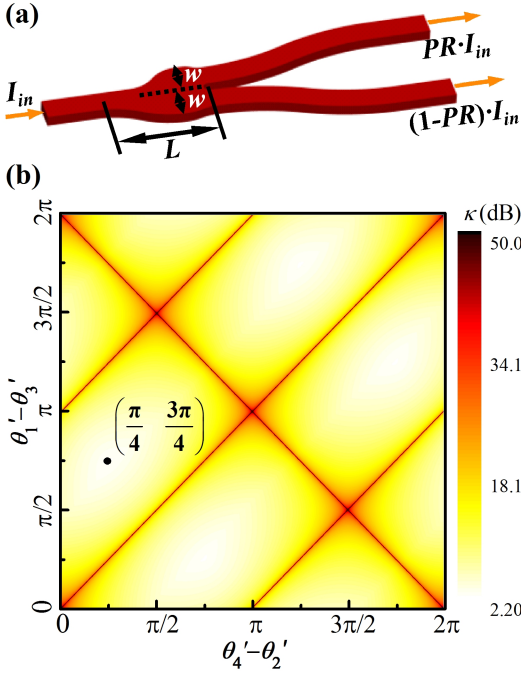

FIG. 10. (a) The schematic of the asymmetrical power splitter. (b) The condition number as a function with $(\theta_1' - \theta_3')$ and $(\theta_4' - \theta_2')$, when $\tau = 2 - \sqrt{3}$. The structure with the parameter of $(\pi/4 \; 3\pi/4)$ was chosen to be fabricated.

V. DISCUSSIONS: NOISE MINIMIZATION

The polarimeter can be regarded as a projector that projects the input Stokes vector onto an intensity vector of measurement[36]. For simplicity, we normalize the analysis matrix $\mathbf{W}$ so that $W_{i1}^2 = W_{i2}^2 + W_{i3}^2 + W_{i4}^2 = 1$, where i means the ith row of the matrix[37]. Therefore, the endpoints of the reduced vectors $\mathbf{w}_i = (W_{i2}, W_{i3}, W_{i4})$ are located on the surface of the Poincaré sphere. The measurement frame (i.e. the set of vectors $\{\mathbf{w}_i\}$) can be described by a polyhedron whose vertexes are defined by the endpoints of the reduced vectors $\mathbf{w}_i$. It has been demonstrated that the Platonic polyhedron can achieve the minimum condition number[38]. Our first proposed SiP-4PD-DOAP (Fig. 2) whose measurement frame is an irregular tetrahedron (as shown in Fig.12a) does not have the minimum condition number. Figure 12b and c show the mea-

surement frames of the polarimeter desgined by Savenkov[35] and our proposed second SiP-4PD-DOAP with APSs (including $\mathbf{W}_b$ and $\mathbf{W}_b'$), respectively. Both of them provide a regular tetrahedron and the minimum condition number. The regular tetrahedron is a spherical 2-design[39] with N=4, which has been proven not able to realize noise variance equalization except for two particular orientations (i.e. the tetrahedrons are shown in Fig. 12c)[36] in the presence of Poisson noise. However, this limitation can be broken via the regular octahedron, which is the simplest spherical 3-design. The regular octahedron presented in Fig. 12d is one example: when rotated to another orientation, it remains such a property[36].

All the polyhedrons shown in Figs. 12c and d can realize a minimal and equalized Poison noise variance, but suffer from different additive Gaussian noise. Here we examine the impact of the detection number N on the total variance of the four Stokes channels (termed as equally weighted variance, EWV). Consider the cases of Platonic polyhedrons. The optical power received by each PD is proportional to S_0/N (i.e. the DOAP, and the division of time polarimeter, DOTP which used in the scenario of "photon-starved"). In these cases, the analysis matrix $\mathbf{W}$ has the following properties:[36]

$$\forall i \; (i = 1, 2, ,, N), \; W_{i1} = \frac{1}{N}, \qquad (16)$$

and

$$\mathbf{W}^T \mathbf{W} = \frac{1}{3N} \begin{pmatrix} 3 & 0 & 0 & 0 \\ 0 & 1 & 0 & 0 \\ 0 & 0 & 1 & 0 \\ 0 & 0 & 0 & 1 \end{pmatrix}, \qquad (17)$$

where $\mathbf{W}^T$ is the transpose of $\mathbf{W}$.

For AWGN, EWV_{add} is given by[40]

$$EWV_{add} = \sigma_n^2 \cdot \mathrm{Tr}\left[\left(\mathbf{W}^T \mathbf{W}\right)^{-1}\right], \qquad (18)$$

where σ_n^2 is the variance of the additive noise, and $\mathrm{Tr}(*)$ means the sum of the elements on the main diagonal (the diagonal from the upper left to the lower right) of $*$. Based on Eq. 17 and 18, we can obtain that

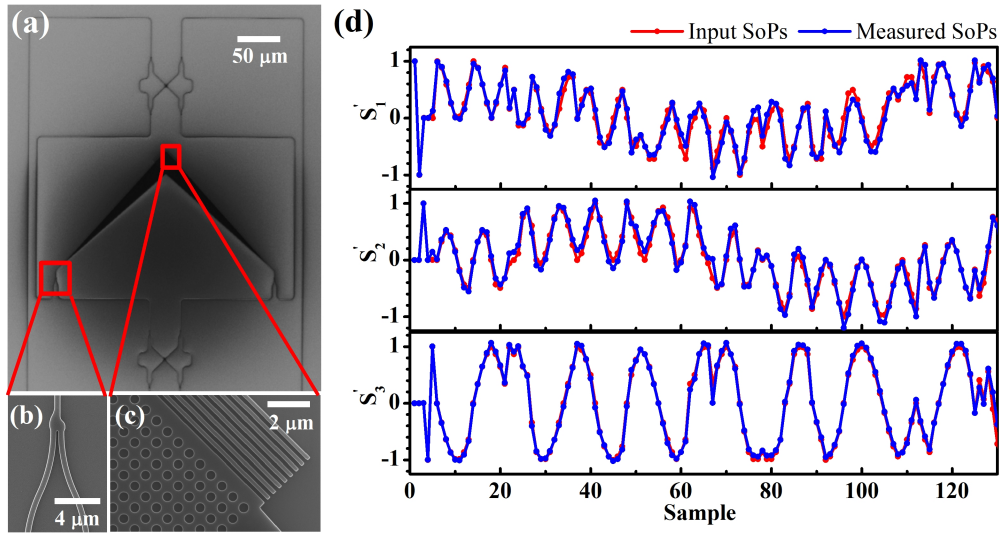$$EWV_{add} = 10N\sigma_n^2. \qquad (19)$$

FIG. 11. (a) is the SEM image of the improved device. (b), and (c) are the enlarged SEM images of APS, and 2-ports SPS, respectively. (d) The measured results of our device and their corresponding input SoPs at the wavelength of 1550 nm.
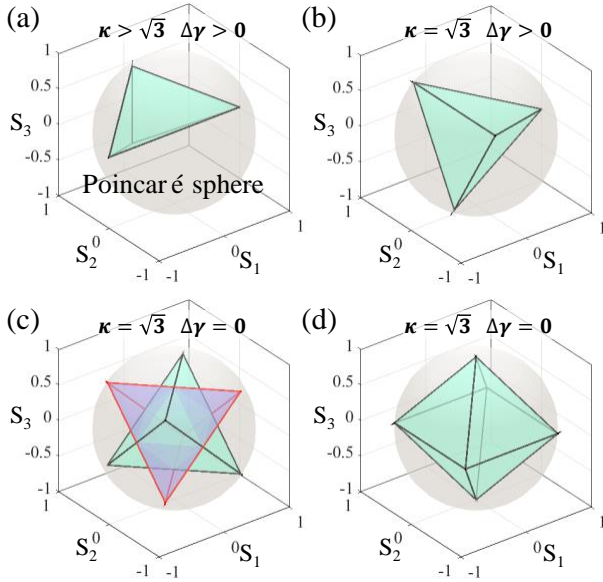

FIG. 12. The measurement frames for (a) the proposed SiP-4PD-DOAP without APS, (b) the polarimeter given by Savenkov[35], (c) the proposed SiP-4PD-DOAP with APS (including $\mathbf{W}_b$ and $\mathbf{W}_{b'}$), and (d) the optimally conditional SiP-6PD-DOAP[21]. The vertexes of the polyhedrons are located on the surface of Poincaré sphere

For Poission noise, EWV_{Poi} has the following expression[40]

$$\text{EWV}_{Poi} = W_{11} \cdot S_0 \cdot \text{Tr}\left[\left(\mathbf{W}^T\mathbf{W}\right)^{-1}\right]. \qquad (20)$$

Based on Eqs. 16, 17 and 20, we can obtain that

$$\text{EWV}_{Poi} = 10S_0. \qquad (21)$$

From Eq. 19, we can know that in the presence of the additive noise, EWV_{add} increases with N. Therefore, the regular

tetrahedrons in the two specific orientations are the best architectures (Fig. 12c and d). On the other hand, Eq. 20 indicates that the EWV_{Poi} is independent of the numbers of PDs. Overall, 4PD-DOAP not only has a relatively low cost in signal processing, but also is less influenced by noise in the reconstruction of SoP. Notice that the conclusion may be opposite for a DOTP, where no power splitting is required and SoP is detected at a relatively low speed[34]. In this case, people usually take more measurements to suppress noise.

VI. CONCLUSION

In conclusion, we have demonstrated, for the first time, a chip-scale, solid-state full-Stokes polarimeter with an optimal frame in presence of both Gaussian and Poisson noises. Two ultra-compact full-Stokes polarimeters with a minimum number of power detection have been proposed and experimentally demonstrated using a CMOS-compatible fabrication process. Their designs were optimized taken into consideration both the condition number and estimation variance. A polarimeter architecture for an optimal 4PD-DOAP analysis matrix ($\mathbf{W}_b$ or $\mathbf{W}_{b'}$) with the minimum condition number ($\kappa = \sqrt{3}$) and Poisson shot noise equalization ($\Delta\gamma = 0$) has been achieved in a PIC for the first time. Excellent agreement has been shown between the measured results using our devices and a bench-top commercial instrument. We show that, within the optimal frames of Stokes polarimeters, increasing the number of detection beyond four through power division causes a higher additive Gaussian noise while the Poisson shot noise is not affected. Therefore, 4PD-DOAP offers a theoretically optimal DOAP design.

Integrated polarimeters are still in the experimental demonstration phase. Comparing performance is difficult due to the wide variation in reported measurement set-ups. For example, our polarimeters are not packaged, and therefore error is

induced both from the measurement set-up and the polarimeter itself. The theoretical optimality of our proposed architecture could be established experimentally vis-á-vis others methods only if the same measurement conditions could be put in place. A summary of recently reported integrated full-Stokes polarimeters is provided in Supplementary Material.

The proposed structures can also be extended to other materials platforms, such as silicon nitride, and germanium for the visible and mid-infrared ranges[20,41]. Furthermore, these compact polarimters can be readily integrated with other silicon photonics devices such as spectrometers[42] so that an comprehensive optical vector analysis can be achieved on a single chip for even broader applications.

VII. FUNDING

VIII. SUPPLEMENTARY MATERIAL

See supplementary material for the previously reported integrated full-Stokes polarimeters.

ACKNOWLEDGMENTS

[1]R. Azzam, "Stokes-vector and mueller-matrix polarimetry," JOSA A **33**, 1396–1408 (2016).

[2]E. Collett, *Field guide to polarization*, Vol. 15 (SPIE press Bellingham, 2005).

[3]A. Chrysostomou, P. W. Lucas, and J. H. Hough, "Circular polarimetry reveals helical magnetic fields in the young stellar object HH 135–136," Nature **450**, 71 (2007).

[4]Y. Li, F. C. Salisbury, Z. Zhu, T. G. Brown, P. S. Westbrook, K. S. Feder, and R. S. Windeler, "Interaction of supercontinuum and Raman solitons with microstructure fiber gratings," Optics express **13**, 998–1007 (2005).

[5]V. T. Saunders, "The polarimeter. a lecture on the theory and practice of polarimetry," Adam Hilger, Ltd. (1939).

[6]R. Azzam, "The intertwined history of polarimetry and ellipsometry," Thin Solid Films **519**, 2584–2588 (2011).

[7]J. B. Mueller, K. Leosson, and F. Capasso, "Ultracompact metasurface in-line polarimeter," Optica **3**, 42–47 (2016).

[8]W. T. Chen, P. Török, M. R. Foreman, C. Y. Liao, W.-Y. Tsai, P. R. Wu, and D. P. Tsai, "Integrated plasmonic metasurfaces for spectropolarimetry," Nanotechnology **27**, 224002 (2016).

[9]N. A. Rubin, A. Zaidi, M. Juhl, R. P. Li, J. B. Mueller, R. C. Devlin, K. Leósson, and F. Capasso, "Polarization state generation and measurement with a single metasurface," Optics express **26**, 21455–21478 (2018).

[10]W. Li, Z. J. Coppens, L. V. Besteiro, W. Wang, A. O. Govorov, and J. Valentine, "Circularly polarized light detection with hot electrons in chiral plasmonic metamaterials," Nature communications **6**, 8379 (2015).

[11]V. Mikhailov, B. A. Rabin, and P. S. Westbrook, "In-line high-speed all-fiber polarimeter with true real-time acquisition for sensor systems based on fast polarization rotation," Journal of Lightwave Technology **33**, 2679–2684 (2015).

[12]A. Espinosa-Soria, F. J. Rodríguez-Fortuño, A. Griol, and A. Martínez, "On-chip optimal stokes nanopolarimetry based on spin–orbit interaction of light," Nano letters **17**, 3139–3144 (2017).

[13]T. Lipka, L. Moldenhauer, J. Müller, and H. K. Trieu, "Photonic integrated circuit components based on amorphous silicon-on-insulator technology," Photonics Research **4**, 126–134 (2016).

[14]Z. Lin, Y. Chen, L. Rusch, and W. Shi, "On-chip circular polarization splitter using silicon photonic nanoantenna array," ACS Photonics **5**, 4338–4342 (2018).

[15]M. Iqbal, M. A. Gleeson, B. Spaugh, F. Tybor, W. G. Gunn, M. Hochberg, T. Baehr-Jones, R. C. Bailey, and L. C. Gunn, "Label-free biosensor arrays based on silicon ring resonators and high-speed optical scanning instrumentation," IEEE Journal of Selected Topics in Quantum Electronics **16**, 654–661 (2010).

[16]K. Xu, "Silicon mos optoelectronic micro-nano structure based on reverse-biased pn junction," physica status solidi (a) **216**, 1800868 (2019).

[17]K. Williams, E. Bente, D. Heiss, Y. Jiao, K. Ławniczuk, X. Leijtens, J. van der Tol, and M. Smit, "InP photonic circuits using generic integration," Photonics Research **3**, B60–B68 (2015).

[18]T. Hu, B. Dong, X. Luo, T.-Y. Liow, J. Song, C. Lee, and G.-Q. Lo, "Silicon photonic platforms for mid-infrared applications," Photonics Research **5**, 417–430 (2017).

[19]A. Rahim, E. Ryckeboer, A. Z. Subramanian, S. Clemmen, B. Kuyken, A. Dhakal, A. Raza, A. Hermans, M. Muneeb, S. Dhoore, *et al.*, "Expanding the silicon photonics portfolio with silicon nitride photonic integrated circuits," Journal of Lightwave Technology **35**, 639–649 (2017).

[20]R. Soref, "Mid-infrared photonics in silicon and germanium," Nature photonics **4**, 495 (2010).

[21]Z. Lin, L. Rusch, Y. Chen, and W. Shi, "Chip-scale, full-Stokes polarimeter," Optics Express **27**, 4867–4877 (2019).

[22]P. Dong, X. Chen, K. Kim, S. Chandrasekhar, Y.-K. Chen, and J. H. Sinsky, "128-Gb/s 100-km transmission with direct detection using silicon photonic stokes vector receiver and I/Q modulator," Optics express **24**, 14208–14214 (2016).

[23]W. Wu, Y. Yu, W. Liu, and X. Zhang, "Fully integrated CMOS-compatible polarization analyzer," Nanophotonics (2019).

[24]R. Azzam, "Division-of-amplitude photopolarimeter (DOAP) for the simultaneous measurement of all four stokes parameters of light," Optica Acta: International Journal of Optics **29**, 685–689 (1982).

[25]Z. Lin and W. Shi, "Broadband, low-loss silicon photonic Y-junction with an arbitrary power splitting ratio," Optics Express **27**, 14338–14343 (2019).

[26]Y. Zhang, S. Yang, A. E.-J. Lim, G.-Q. Lo, C. Galland, T. Baehr-Jones, and M. Hochberg, "A compact and low loss Y-junction for submicron silicon waveguide," Optics express **21**, 1310–1316 (2013).

[27]J. S. Tyo, "Design of optimal polarimeters: maximization of signal-to-noise ratio and minimization of systematic error," Applied optics **41**, 619–630 (2002).

[28]D. Sabatke, M. Descour, E. Dereniak, W. Sweatt, S. Kemme, and G. Phipps, "Optimization of retardance for a complete Stokes polarimeter," Optics Letters **25**, 802–804 (2000).

[29]F. Goudail, "Noise minimization and equalization for Stokes polarimeters in the presence of signal-dependent Poisson shot noise," Optics letters **34**, 647–649 (2009).

[30]A. Mekis, S. Gloeckner, G. Masini, A. Narasimha, T. Pinguet, S. Sahni, and P. De Dobbelaere, "A grating-coupler-enabled CMOS photonics platform," IEEE Journal of Selected Topics in Quantum Electronics **17**, 597–608 (2010).

[31]Y. Zhang, S. Yang, Y. Yang, M. Gould, N. Ophir, A. E.-J. Lim, G.-Q. Lo, P. Magill, K. Bergman, T. Baehr-Jones, *et al.*, "A high-responsivity photodetector absent metal-germanium direct contact," Optics express **22**, 11367–11375 (2014).

[32]C. T. DeRose, D. C. Trotter, W. A. Zortman, A. L. Starbuck, M. Fisher, M. R. Watts, and P. S. Davids, "Ultra compact 45 GHz CMOS compatible germanium waveguide photodiode with low dark current," Optics express **19**, 24897–24904 (2011).

[33]M. Ye, Y. Yu, J. Zou, W. Yang, and X. Zhang, "On-chip multiplexing conversion between wavelength division multiplexing–polarization division multiplexing and wavelength division multiplexing–mode division multiplexing," Optics letters **39**, 758–761 (2014).

[34] A. Peinado, A. Lizana, J. Vidal, C. Iemmi, and J. Campos, "Optimization and performance criteria of a Stokes polarimeter based on two variable retarders," Optics express **18**, 9815–9830 (2010).

[35] S. N. Savenkov, "Optimization and structuring of the instrument matrix for polarimetric measurements," Optical Engineering **41**, 965–973 (2002).

[36] F. Goudail, "Equalized estimation of stokes parameters in the presence of poisson noise for any number of polarization analysis states," Optics letters **41**, 5772–5775 (2016).

[37] M. R. Foreman and P. Török, "Information and resolution in electromagnetic optical systems," Physical Review A **82**, 043835 (2010).

[38] M. R. Foreman, A. Favaro, and A. Aiello, "Optimal frames for polarization state reconstruction," Physical review letters **115**, 263901 (2015).

[39] R. Hardin and N. Sloane, "Spherical designs, a library of putatively optimal spherical t-designs," URL http://www. research. att. com/˜ njas/sphdesigns (2002).

[40] J. Dai, F. Goudail, M. Boffety, and J. Gao, "Estimation precision of full polarimetric parameters in the presence of additive and poisson noise," Optics express **26**, 34081–34093 (2018).

[41] D. J. Moss, R. Morandotti, A. L. Gaeta, and M. Lipson, "New CMOS-compatible platforms based on silicon nitride and hydex for nonlinear optics," Nature photonics **7**, 597 (2013).

[42] H. Wang, Z. Lin, Q. Li, and W. Shi, "On-chip fourier transform spectrometers by dual-polarized detection," Optics Letters **44**, 2923–2926 (2019).